Toward scene-based retrieval of spectral response functions for hyperspectral imagers using Fraunhofer features

Jason Brazile, Robert A. Neville, Karl Staenz, Daniel Schläpfer, Lixin Sun, and Klaus I. Itten

Abstract. Initial steps are proposed and tested in the development of a method for retrieving and (or) refining instrument spectral characteristics for dispersive hyperspectral imagers such as the Airborne Visible / Infrared Imaging Spectrometer (AVIRIS), Compact Airborne Spectrographic Imager (*casi*), HyMap, Hyperion, and compact high-resolution imaging spectrometer (CHRIS) based on data acquired by the instrument in operation using statistical spectrum matching with moderate-resolution transmittance code (MODTRAN) modelled instrument results in the vicinity of reference Fraunhofer feature windows. Until now, such scene-based retrieval has focused primarily on refining spectral band-centre shifts while assuming that spectral response function (SRF) parameters remain static. In particular, most methods assume that the SRF is of a Gaussian shape. As a consequence of recent investigations showing that scene-based discernment of SRF shape should be feasible given current typical instrument performance, this paper explores algorithmic components deemed necessary for the development of a look-up table (LUT) based retrieval method for obtaining SRF parameters on a band-by-band basis, even in the presence of minor band-centre or bandwidth deviations from nominal instrument specifications. The proposed method employing these components is appropriate for dispersive hyperspectral imagers but not for others, for example Fourier transform hyperspectral imagers. In experiments using nominal implementations of the proposed components, reference spectra match expected LUT spectra in nearly all cases, even when band-centre and bandwidth deviations are considered. This holds true for all three modelled instruments and nearly all of the six selected Fraunhofer windows. Expected signal-to-noise requirements are in many cases challenging, yet feasible using signal-enhancement techniques such as along-track averaging.

Résumé. On propose et teste les étapes initiales dans le développement d'une méthode pour l'extraction et raffinement des caractéristiques spectrales pour les imageurs hyperspectraux dispersifs tels que le spectromètre AVIRIS (« Airborne Visible / Infrared Imaging Spectrometer »), *casi* (« Compact Airborne Spectrographic Imager »), HyMap,, Hyperion et CHRIS (« compact high-resolution imaging spectrometer ») basé sur des données acquises par l'instrument en mode opératoire à l'aide de l'appariement statistique des spectres avec des résultats de l'instrument en question modélisés par MODTRAN (« moderate-resolution transmittance code ») dans le voisinage des fenêtres de référence de Fraunhofer. Jusqu'à maintenant, ce type d'extraction basé sur les images s'est intéressé principalement au raffinement des déplacements du centre des bandes spectrales en assumant que les paramètres de la fonction de réponse spectrale (SRF) demeure statique. En particulier, la plupart des méthodes assument que la SRF est de forme gaussienne. Suite à des recherches récentes montrant que le discernement basé sur des images de la forme de la SRF serait efficace, étant donné la performance typique actuelle des instruments, dans cet article on explore les composantes algorithmiques jugées nécessaires pour le développement d'une méthode basée sur une table de visualisation (LUT) pour l'obtention des paramètres SRF bande par bande, même en présence d'écarts mineurs du centre de la bande ou de la largeur de la bande par rapport aux spécifications nominales des instruments. La méthode proposée utilisant ces composantes est adéquate pour les imageurs hyperspectraux dispersifs mais pas pour les autres, par exemple les imageurs hyperspectraux basés sur le transformée de Fourier. Dans des expériences utilisant des implémentations nominales des composantes proposées, les spectres de référence correspondent aux spectres LUT dans la plupart des cas, même lorsque les écarts du centre de la bande ou de la largeur de la bande sont pris en considération. Ceci demeure vrai pour les trois instruments modélisés ainsi que pour presque toutes les six fenêtres Fraunhofer choisies. Les spécifications visées au niveau du rapport signal sur bruit posent des défis dans de nombreux cas, mais elles sont atteignables en utilisant des techniques de rehaussement du signal, telle que le calcul de la moyenne le long de la trace.
[Traduit par la Rédaction]

J. Brazile,[1] D. Schläpfer, and K.I. Itten. Remote Sensing Laboratories, University of Zurich, Winterthurerstrasse 190, CH-8057 Zurich, Switzerland,

R.A. Neville, K. Staenz,[2] and L. Sun. Canada Centre for Remote Sensing, Natural Resources Canada, 588 Booth Street, Ottawa, ON K1A 0Y7, Canada.

[1]Corresponding author (e-mail: jason.brazile@geo.uzh.ch).
[2]Present address: Alberta Terrestrial Imaging Centre, University of Lethbridge, 401, 817 4th Avenue South, Lethbridge, AB T1J 0P3, Canada.

Introduction

Motivation

As the use of hyperspectral imaging data for a wide range of applications becomes more widespread, expectations increase with regard to the resolution and accuracy of such data. In particular, erroneous spectral calibration, i.e., the assignment of spectral wavelengths to the recorded across-track pixel number, can lead to large errors in the resulting generated surface reflectance products required by a majority of earth observation applications. Spectral calibration is performed in the laboratory either pre-launch as with the Hyperion spaceborne instrument (Pearlman et al., 2003) or between flight seasons in the case of airborne instruments such as the Airborne Visible / Infrared Imaging Spectrometer (AVIRIS) (Green et al., 1988), in which multiple calibrations are possible. Laboratory calibration typically involves using a monochromator to scan across the focal plane in sub-nanometre steps (Cocks et al., 1998). Another method involves using a tuneable etalon filter, allowing multiple measurements to be taken simultaneously and enabling calibration over larger portions of the detector array and with different look angles (Sinclair et al., 2002). More recently, a laboratory-based spectral response function (SRF) estimation method has been described using the same low-pressure gas lamps as those used in the calibration of the instrument band centre (Milton and Choi, 2004).

There are various reasons why scene-based calibration is desirable. When used to refine traditional laboratory characterization, it can help determine conditions when intensive recharacterization or recalibration is called for, such as instrument deterioration over time or deployment in new environments. For some characterizations where results are deemed effective enough, it could be used in lieu of more traditional methods. Laboratory calibration is very resource intensive. Some instruments, such as the Compact Airborne Spectrographic Imager (*casi)* (Anger et al., 1996), allow multiple configurations (Milton, 2006), each preferably with its own characterization. In extreme cases, such as the Airborne Prism Experiment (APEX) spectrometer (Itten et al., 1997), summing the entire set of subchannels (511) of the instrument is fully programmable, allowing arbitrary data-take-specific configurations (Schaepman and Itten, 1998). Additionally, increased interest in spectrodirectional spectroscopy implies that multi-angular instruments such as the compact high resolution imaging spectrometer (CHRIS) (Barnsley et al., 2004) might become more common, multiplying calibration complexity for each view angle. Lastly, perhaps the most attractive argument for scene-based characterization is that it can be performed by anyone in possession of a suitable dataset. One can attempt to retrieve or refine instrument characteristics at the time of any particular data-take.

Scene-based detection of instrument characteristics also has disadvantages. The methods employed are typically complicated and might be fragile in untested situations. They can also be computationally intensive, though this may be less costly than deployment and maintenance of traditional laboratory retrieval methods, especially when initial software development and hardware costs are amortized over time. Most critically, scene-based methods have been suspected of producing results inferior to those from traditional methods. However, the expected trend is that growing confidence as techniques mature will cause this perception to diminish over time.

Scene-based retrieval

It is becoming increasingly more feasible to retrieve and (or) refine instrument characteristics in hyperspectral imaging data by analyzing the data themselves. Gao et al. (2002) introduced and later refined (Gao et al., 2004) a spectrum-matching technique to improve data calibration. Ramon et al. (2003) and Casadio and Colagrande (2004) performed similar calibration for the spaceborne medium-resolution imaging spectrometer (MERIS) based on the O-absorption feature. Neville et al. (2003) also used a feature-based method specifically for the detection of spectral line curvature that subsequently inspired a method for the scene-based detection of keystone aberrations (Neville et al., 2004). Although the accuracy of these spectrum-matching techniques relies on the correctness of a trusted model, such as that provided by the atmospheric radiative transfer (RT) code MODTRAN 4 (Berk et al., 1998) and its high-resolution transmission molecular absorption (HITRAN) based feature database (Rothman et al., 2003), so too does the atmospheric correction of the scene, and therefore the end product itself. Accordingly, consistency is maintained, provided the same trusted model is used for generation of look-up table (LUT) entries for both the atmospheric correction and the characterization via spectrum matching. Further, it is argued that both instrument characterization and the resulting surface reflectance products become more accurate as the trusted model becomes more accurate.

The most difficult and error-prone process in deriving end-user products from remotely sensed earth observation data involves atmospheric correction. Three of the most important instrument parameters used as inputs for atmospheric correction, i.e., for generating surface reflectance products from at-sensor radiance, are per-band band centres, bandwidths (typically characterized as full width at half-maximum (FWHM)), and SRF shape. The aforementioned studies have explored retrieval of band-centre and bandwidth parameters. Therefore, the next step is to investigate methods for the scene-based retrieval of per-band SRF shapes.

The theoretic feasibility of discernment of a set of given SRFs from the typically used Gaussian has recently been established (Brazile et al., 2006) specifically for the case of the APEX imaging spectrometer currently being built (Nieke et al., 2005). Band-by-band SRF retrieval feasibility was addressed by examining sensitivity of discernment using spectrum matching of several different Fraunhofer feature windows across a wide spectral range, and under varying target reflectances and aerosol visibility conditions. However, this

work stopped short of defining a general scene-based per-band SRF retrieval method.

The goal of this paper is to extend this work by exploring and validating specific components required for a generally applicable scene-based SRF retrieval method. In particular, these components should include the following: (*i*) an SRF parameterization should be established that generates realistic shapes and is continuous enough to allow retrieval via spectrum matching against discrete LUT entries; (*ii*) a robust spectrum-matching metric needs to be possible, even in the presence of minor shifts in nominal band centre and (or) changes in bandwidth specifications; (*iii*) spectral coverage should include a large enough set of Fraunhofer features that are prominent enough to reveal discernible signal differences in the resulting at-sensor radiances throughout the spectral range of an instrument; (*iv*) general applicability should be established by testing for multiple instruments; and (*v*) statistical consistency should reveal trends in neighbouring bands, allowing the identification and rejection of outliers.

Method

The proposed method, consisting of nominal implementations of the proposed components, attempts to simulate the steps needed to match the reference spectra produced from a specific data-take by a specific instrument against a large pregenerated set of trial spectra modelled from the specifications of that instrument but allowing its nominal spectral characteristics to vary. The assumption is that when a good match is found between the reference spectra and one of the pregenerated spectra, chances are good that the spectral characteristics of the instrument that produced the reference spectra are reflected by the input parameters used for generating the matching LUT entry. It is assumed that

interpolation can be used to fill in the gaps between LUT entries, at least in mathematically well-behaved situations.

The process is centred around the characteristic issue appearing both during the forward modelling of the instrument under varying spectral characteristics and indirectly in the inverse modelling of the matching spectra. This is the question of how to model the SRF. First, an attempt was made to define the properties desirable for an SRF model. Initially, it was thought that functions with well-defined formulas for determining properties, such as area or FWHM, would be useful for ease in generation and intercomparison of SRFs. An earlier study (Brazile et al., 2006) proposed apodization functions (Weisstein, 2005) such as Welch or cosine to fulfil this requirement. However, it became clear that, for retrieval purposes, it is more important for an SRF to have a parameterized, smoothly changing nature, which preferably covers a variety of known shapes.

A search of the literature revealed the Tukey function (Harris, 1978), which in its parameterization ranges from equivalence with the boxcar to equivalence with the Hann function (**Figure 1**). Although its continuous nature seems ideal, initial investigation indicated that its Hann extreme did not go far enough toward the typically used Gaussian shape to cover cases that appear in practice (**Figure 2**).

It was decided that an appropriate parameterization could be obtained by summing a number of Gaussians at varying ratios of subchannel FWHM to spectral sampling interval (SSI). Physically, the summing of Gaussians corresponds to the common practice of summing instrument subchannels to increase per-band signal-to-noise ratio (SNR) performance. Through examination of the resulting shapes, it was decided to allow the number of summed Gaussians to vary among 1, 2, 4, 6, and 8 and the subchannel FWHM to SSI ratios to vary in six linear steps, namely 1.30, 1.44, 1.58, 1.72, 1.86, and 2.00 (**Figure 1**).

Figure 1. Shape coverage of candidate spectral response function (SRF) parameterization models. (a) Tukey fails to cover shapes from Hann to Gaussian. (b) The 2, 4, 6, and 8 summed Gaussians, each with FFWH:SSI of 1.3, 1.44, 1.58, 1.72, 1.86, and 2 (i.e., 6 linear steps).
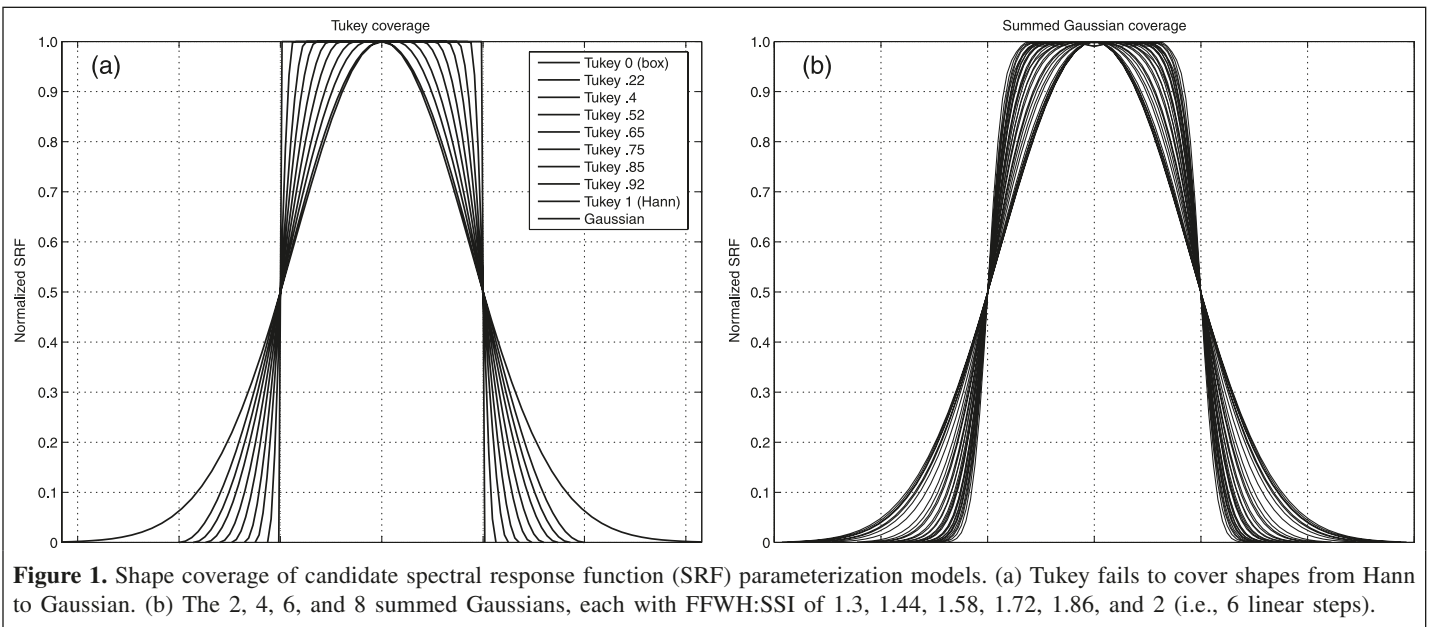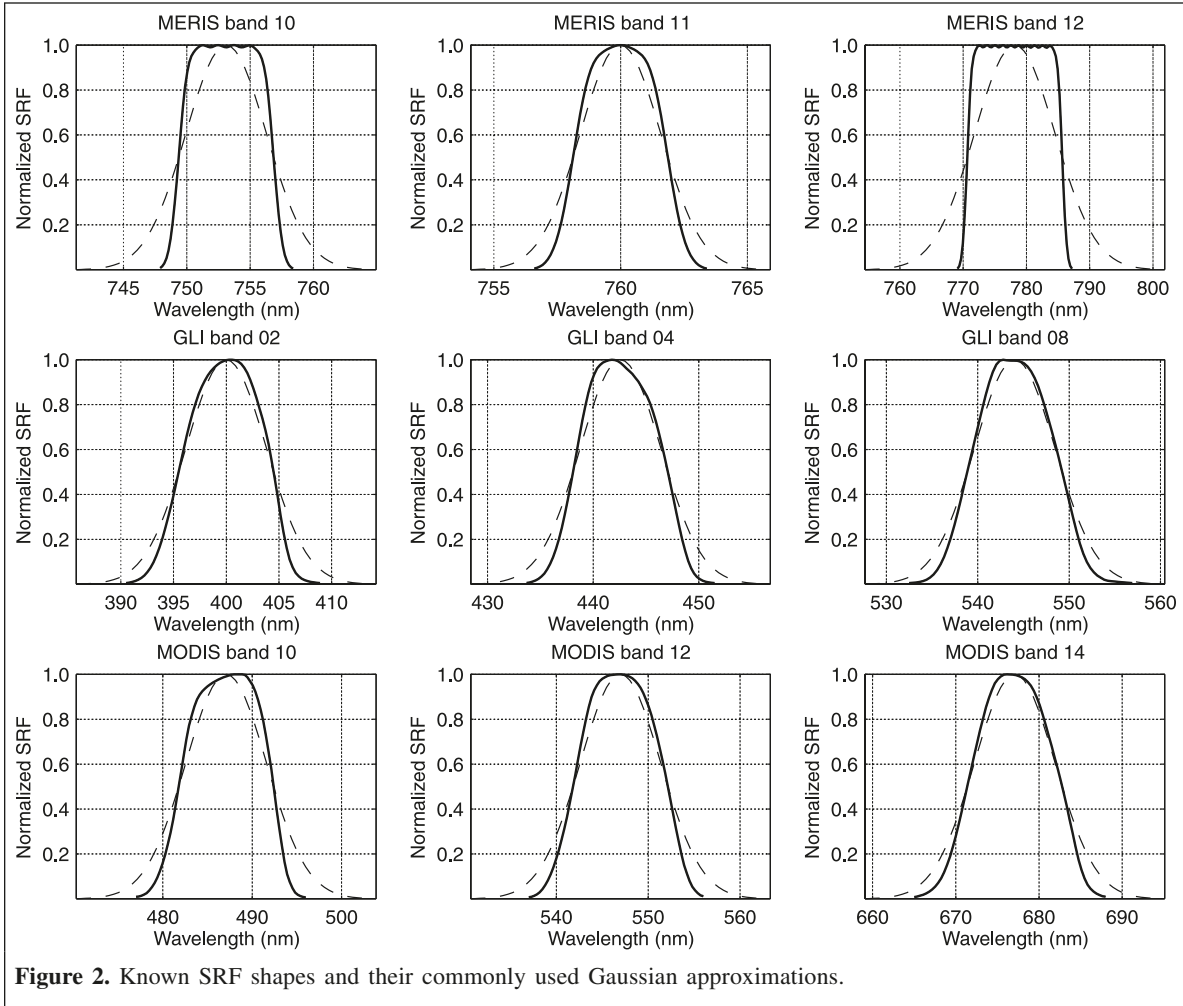
Figure 2. Known SRF shapes and their commonly used Gaussian approximations.

If the SRF of the subchannels covered by a summed band can be assumed to be a Gaussian function (g_i), then the SRF of the summed band can be expressed by summing the SRFs of all the covered subchannels as follows:

$$\text{SRF}_{\text{sum}(\lambda)} = \sum_{i=1}^{N} g_i(\lambda) \tag{1}$$

$$g_i(\lambda) = \exp\left[-\frac{4\ln(2)(\lambda - \mu_i^{\text{sub}})^2}{\text{FWHM}_{\text{sub}}^2}\right] \tag{2}$$

where FWHM_{sub} is the FWHM of the subchannels (assumed to be the same over the given span), μ_i^{sub} is the centre wavelength position of the ith subchannel relative to the centre wavelength of its corresponding summed band, λ is the sample wavelength, and N is the number of subchannels. FWHM_{sub} and μ_i^{sub} can be calculated using the following formulas:

$$\text{FWHM}_{\text{sub}} = R \cdot \text{SSI}_{\text{sub}} \tag{3}$$

$$\mu_i^{\text{sub}} = \{C_{\text{sum}} - [(N-1)\,\text{SSI}_{\text{sub}}]\}(i-1)\,\text{SSI}_{\text{sub}} \tag{4}$$

where $\text{SSI}_{\text{sub}} = \text{SSI}_{\text{sum}}/N$ (if the SSI between two adjacent summed bands is known or can be assumed), R is the ratio of FWHM_{sub} to SSI_{sub}, SSI_{sub} is the spectral sampling interval between the centres of two adjacent subchannels, SSI_{sum} is the spectral sampling interval of the summed band, and C_{sum} is the centre wavelength of a given summed band.

The resulting implementation of Equation (1) is normalized, ensured to fit the specific band-centre location of the summed band, and down-sampled to 65 samples to conform to the MODTRAN input filter convention. In essence, this routine is similar to the previously used filter generator (Brazile, 2005) but augmented to allow for the additional summing and ratio parameters.

It is now possible to examine the experimental method in detail. An overview of the process is visualized in the flow diagram in **Figure 3**. There are three general phases of the experiment: (*i*) pregeneration of instrument-specific trial spectra allowing the spectral characteristics of the instrument to vary, (*ii*) generation of reference spectra simulating a particular data-take, and (*iii*) finding the pregenerated spectra that best match the reference and evaluating the match for retrieval purposes.

Figure 3. Overview of experimental method.

file (with the ".flt" suffix, by convention) containing tables of floating point values representing per-band SRFs. Therefore, in the setup of MODTRAN 4 input, the various SRF ".flt" files must first be generated. To this end, a multiply-nested loop "wrapper" around the function corresponding to Equation (1) is used to generate SRFs with instrument-specific but varying spectral characteristics.

Individual input files (MODTRAN "tape5" files) for all runs are then generated referring to the previously created external ".flt" files but otherwise with base input parameters as shown in **Table 1**. To reduce the size of the LUT for this experiment, visibility and target reflectance are not allowed to vary, since a previous study (Brazile et al., 2006) implies that outcomes due to variations in these parameters do not cause substantial changes in the sensitivity of the result and the primary focus of this study is to examine varying SRFs.

The individual simulations are then run on a cluster of Advanced Micro Devices (AMD) Opteron-based compute nodes (Godknecht and Bolliger, 2004) executing all of the thousands of runs. Upon completion of the MODTRAN jobs, the instrument-specific at-sensor radiance spectra in individual "channels.out" files are collected and composed into a single LUT whose dimensions correspond to those of the retrieval parameters shown in **Table 2**.

A second phase of the experiment is to produce reference at-sensor radiance spectra simulating an instrument data-take. The spaceborne sensors Hyperion and CHRIS and the airborne HyMap instrument are considered for this study. This is done by again using MODTRAN 4 to generate the reference spectra.

Table 1. Selected MODTRAN 4 input parameters.

Target reflectance	0.2
Aerosol model	Rural extinction
Visibility	100 km
Atmospheric model	Mid-latitude summer
Surface altitude	400 m
Solar zenith angle	180°
Scattering algorithm	ISAAC two-stream
Solar data	Thuillier (Thuillier et al., 2003)
Filter response function	See text

Table 2. Proposed instrument-specific LUT parameters for retrieval.

Target reflectance
Aerosol model
Visibility
Atmospheric model
Surface altitude
Sensor altitude
Solar zenith angle
No. of summed subchannels[a]
Ratio of subchannel FWHM to SSI[a]
Band-centre shift from nominal[a]
FWHM shift from nominal[a]

[a]Only these parameters varied in this experiment.

Since all modelled at-sensor radiance spectra are produced by the MODTRAN 4 radiative transfer (RT) code from the 20% spectrally flat target reflectance input, the ordering of some of the steps in the procedure is determined by the requirements of this software. For example, MODTRAN 4 allows the input of an arbitrary SRF by setting the "CARD 1A3 FLTNAM" parameter (Berk et al., 2003), which references an external American standard code for information interchange (ASCII)

Table 3. Instrument specifications (in nm) per feature window.

	CHRIS			HyMap			Hyperion		
	$\Delta\lambda$	$\overline{SSI}$	$\overline{FWHM}$	$\Delta\lambda$	SSI	$\overline{FWHM}$	$\Delta\lambda$	SSI	$\overline{FWHM}$
d(Fe)	29.60	9.87	9.68	44.10	14.70	15.42	30.52	10.17	11.39
D1/D2(Na)	31.00	10.33	10.62	46.00	15.33	16.05	30.53	10.18	10.70
a(O)	27.70	9.23	9.20	46.00	15.33	16.15	30.53	10.18	10.39
C(H)	30.90	10.30	10.30	45.60	15.20	16.05	30.52	10.17	10.30
B(O)	17.30	5.77	5.75	45.90	15.30	16.32	30.53	10.18	10.37
A(O)	21.30	7.10	7.08	45.10	15.03	16.45	30.53	10.18	10.73

The aforementioned formula (Equation (1)) is reused to produce reference SRFs. A benefit of using even-numbered summed Gaussians for SRF parameterization during generation of the LUT allows the use of odd-numbered summed Gaussians to generate similar but differing reference cases for validation. For each of the three instruments, 18 validating reference spectra are generated and evaluated at each of six Fraunhofer feature windows, yielding a total of 324 samples for valuation. For generating the reference spectra, nonshifted SRFs are modelled varying over the same six SSIs in the LUT but with summed Gaussians of three, five, and seven rather than the even-summed Gaussians in the LUT. It was decided that these combinations tested on each of the three instruments for different feature windows are minimally required to evaluate retrieval feasibility. A more complete validation of the SRF parameterization and the method itself would involve testing fewer quantized samples over the entire LUT parameter space.

The third phase of the experiment involves the spectrum matching itself and evaluation of the matches for the purpose of retrieval. Spectrum matching is performed using Fraunhofer feature windows of four bands (two on each side of the feature) with the reasoning that perturbations caused by the absorption features increase the likelihood of discerning differences in the SRF-convolved spectra. Instrument specifications in the vicinity of these features are shown in **Table 3**. In practice, more than four bands are sometimes necessary to cover wide absorption features (e.g., 940 nm H_2O). Additionally, absorption features other than these six are usable, and possibly even more appropriate for a particular instrument, but these are the only six that can be uniquely covered by individual windows of four bands for each of the three instruments chosen, allowing for intercomparison.

The evaluation metric for spectrum matching chosen for this experiment is the relative root mean square (rRMS, in %), calculated as follows for a reference window of radiances, L_R, and a second window of radiances L_X:

$$rRMS = \frac{\sqrt{\dfrac{\sum\limits_{i=1}^{n}(L_{Ri} - L_{Xi})^2}{n}}}{\overline{L_{Ri}}} \times 100 \qquad (5)$$

This metric has the merit of directly implying nominal SNR values (i.e., SNR = 100/rRMS) needed to achieve discernment and allowing direct comparison with previous studies also using this metric (Brazile et al., 2006). However, to provide an additional estimation of SNR requirements, multiple amounts of simulated noise are added to the signal in discrete steps corresponding to SNRs of 500:1, 1 000 : 1, 5 000 : 1, 10 000 : 1, and 50 000 : 1. In particular, a vector of uniform random noise N at a given signal-to-noise ratio r was added to the modelled radiance spectra S as described by

$$\vec{S}_n = \vec{S} + \left(\frac{\vec{S}}{r} \times \vec{N}\right) \qquad (6)$$

These noisy spectra are used to determine conservative requirements in the following manner: the differences between rRMS results with noisy spectra and those with no noise are calculated and then characterized by mean and standard deviation. These characterizations are then compared with the difference between the best rRMS and the next-best rRMS result (as calculated without noise). If the difference between these two values is greater than the characterized difference with the given simulated SNR, then it is assumed that SNR performance is sufficient for retrieval. It is argued that the chosen SNRs are challenging but achievable. Since signal-to-noise typically improves by the square root of the number of samples taken (Smith, 1997), one can double the SNR of a single sample by averaging four samples when viewing a relatively homogeneous target.

Given that the target in a scene is varying, the atmosphere is relatively uniform, so the shape of the absorption features remains relatively constant throughout the scene, provided there are no large topographical variations, which might result in significant variability in atmospheric depth. Thus, scene variability provides (to a good approximation) a varying gain factor to all the spectral bands that span the absorption feature. One can therefore gain SNR by averaging increasingly more along-track samples. If the single-pixel SNR is 200:1, and one needs 8 000 : 1, then 1600 along-track samples are needed. For calibration purposes, one should easily be able to obtain 6000 image lines in a scene, which for this example would give an SNR of >15 000 : 1. If more lines are needed, a special calibration data acquisition (assuming a satellite sensor) can be performed over a large desert area (this would give a bright target that itself improves the SNR of each single sample) to

give 50 000 image lines. This could translate to an SNR of ~45 000 : 1 if each single sample SNR is 200:1.

It should be noted that each of the goals stated in the previous section is addressed by the experimental method. A suitable SRF parameterization is introduced that is able to generate realistic shapes and is at least somewhat continuous throughout its range. To address the goal of spectrum-matching robustness in the presence of band-centre or bandwidth deviations, i.e., to enable retrieval–refinement of the spectral line curvature of an instrument, two dimensions are present in the LUT, namely one for allowing up to two discrete band-centre shifts to the left or right in steps of 0.2 nm, and the other for allowing up to two discrete smaller or larger bandwidth changes in steps of 0.5 nm. The experiment attempts to address the spectral coverage issue by testing a selection of Fraunhofer features likely to be prominent enough to be useful with current instruments (Neville, 2003). Interpolation of neighbouring windows could be used to cover gaps in the spectral range of an instrument, but certainly more than a few band windows should be directly covered.

For addressing the goal of general applicability, the experiment is performed on models of three existing instruments with different spectral characteristics, namely the CHRIS and Hyperion spaceborne instruments and the HyMap airborne instrument. Each instrument is modelled using known characteristics such as nominal band centres and sensor altitude. These three instruments are chosen primarily because of the availability of their band specifications, but additionally because their per-band SRFs are not provided, i.e., these are the

kinds of instruments where such a retrieval would be desired. The final goal of statistical consistency is intended to be shown by the results of the experiment.

The modelled trial at-sensor radiance spectra LUT entries resulting from the 625 per-instrument permutations ([(4 summings × 6 subchannel FWHM to SSI ratios) + Gaussian] × 5 band-centre positions × 5 bandwidth values) can be seen for the Fraunhofer A(O) feature in **Figure 4**. Lastly, **Figure 5** shows the relationship between the 625 permutations (bottom row) and the varying LUT input parameters (top four rows). For example, it is clear from the fourth row showing the span of summing cases that the summing parameter is the slowest varying parameter (i.e., the outermost loop) during generation of the LUT. The five summing cases (the smallest sum of one, which has no subchannel ratio variation, is on the right) are easily recognizable.

Results

The spectrum-matching result across all instruments and feature windows for one of the least successfully matching 18 SRF cases is shown in **Figure 6**, and the statistics for the complete set of 324 evaluation samples are characterized in **Table 4**. **Figure 6** plots the spectra-matching metric, i.e., rRMS for all LUT permutations for a given instrument (columns) and Fraunhofer feature window (rows). **Figure 7** shows SNR requirements implied by the rRMS for two extreme cases shown in **Figure 6**, and **Table 5** shows less precise and more conservatively calculated SNR requirements based on

Figure 4. Varying instrument-specific LUT spectra for A(O) feature window.

Figure 5. Relative RMS (rRMS) versus case number. Relationship between case numbers and LUT input parameters.
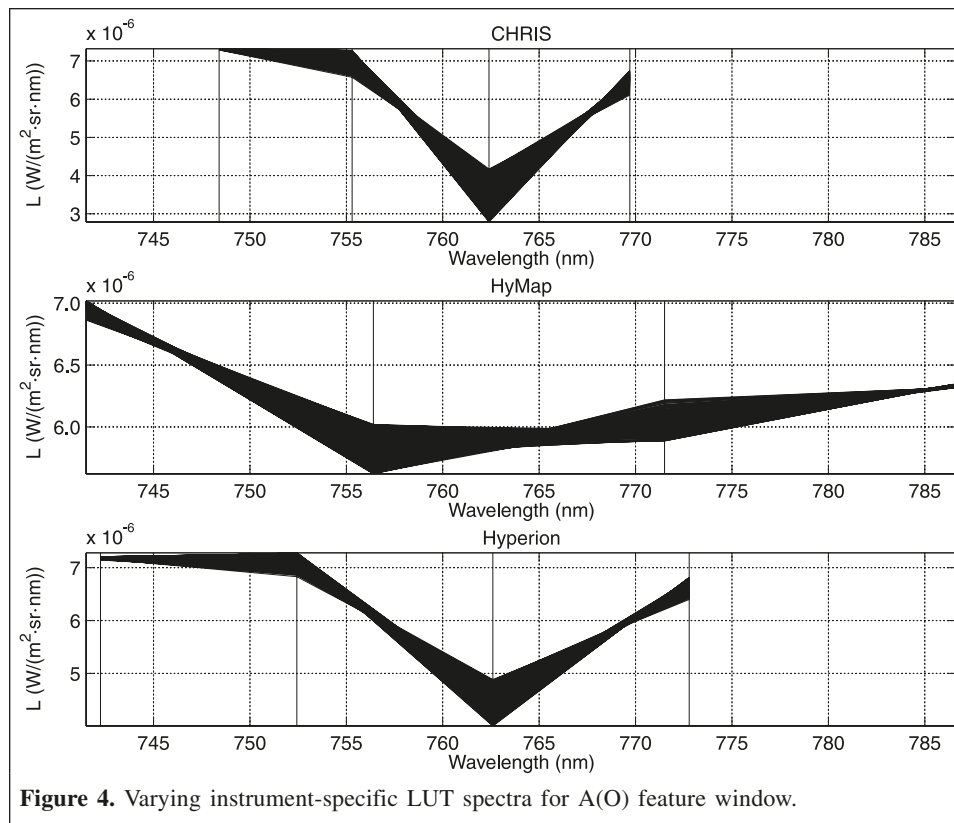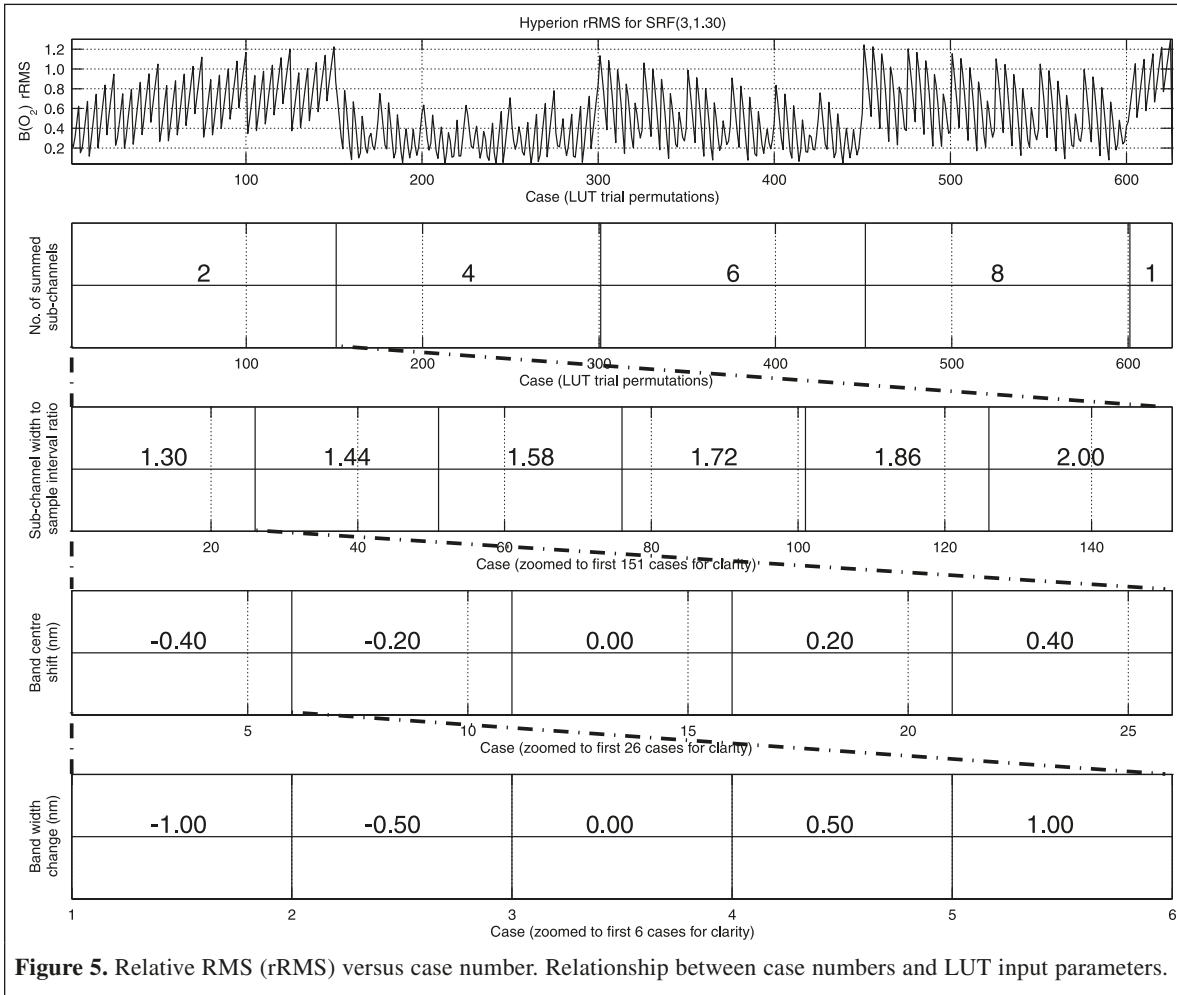
characterized differences when adding simulated noise in discrete steps. The effect of this simulated noise on rRMS can be seen visually in **Figure 8**.

Clear patterns can be seen in **Figure 6**, as entries are allowed to vary in parameters such as band-centre or FWHM shifts, number of summed Gaussians, or subchannel FWHM to SSI ratio. The best matching entry in each plot is marked with a vertical line. The row corresponding to the D1/D2(Na) feature window in the CHRIS column disagrees with all the others. Similarly, the results for the best match in the HyMap column are split, with only the bottom three features agreeing on the best match.

It is also apparent from **Figure 6** that some features provide more clear discernment than others: the C(H) feature shows prominent spikes in each varying group, and the A(O) feature provides the largest rRMS magnitudes.

Again, **Table 4** characterizes the matching statistics for the set of 324 evaluation samples. The result in the table for a particular sample is not shown if it falls into one of two situations. First, if it not clear from the data what the best match should be because the matching results are split, then the entire instrument-specific column for that reference point is left blank. An example of this situation appears in the first HyMap

column for the reference corresponding to the SRF generated from three binned Gaussians and an FWHM to SSI ratio of 1.30. This can be visually verified by looking at the HyMap column in **Figure 6**. In this column, only half of the features (i.e., the bottom three) agree on the match. Therefore the entire column in the corresponding table (column 1, row 4) is left blank.

The second situation occurs when the best match is not the one agreed upon by the other features. In this case, the datum for the given evaluation sample is replaced by an em-dash (—). An example of this case occurs with the D1/D2(Na) feature of the first case (3, 1.30) in the CHRIS result. Again this can be visually verified in **Figure 6** by looking at the CHRIS column and noticing that the best match in the second row disagrees with the best match of all the other features. The corresponding table entries for the mean and standard deviation of that case (column 1, row 1, D1/D2(Na)) are replaced with an em-dash. Entries in **Table 5** corresponding to entries in **Table 4** are also treated the same way with respect to missing entries.

Table 4 reveals that many of the characteristics present in the example graph also hold for the other trials. For example, the A(O) feature often provides the largest variance and mean rRMS values in all trials, and the D1/D2(Na) feature could

Figure 6. Evaluation of matching reference SRF (3, 1.30) against LUT entries using rRMS. The vertical line in each plot denotes the best matching entry.
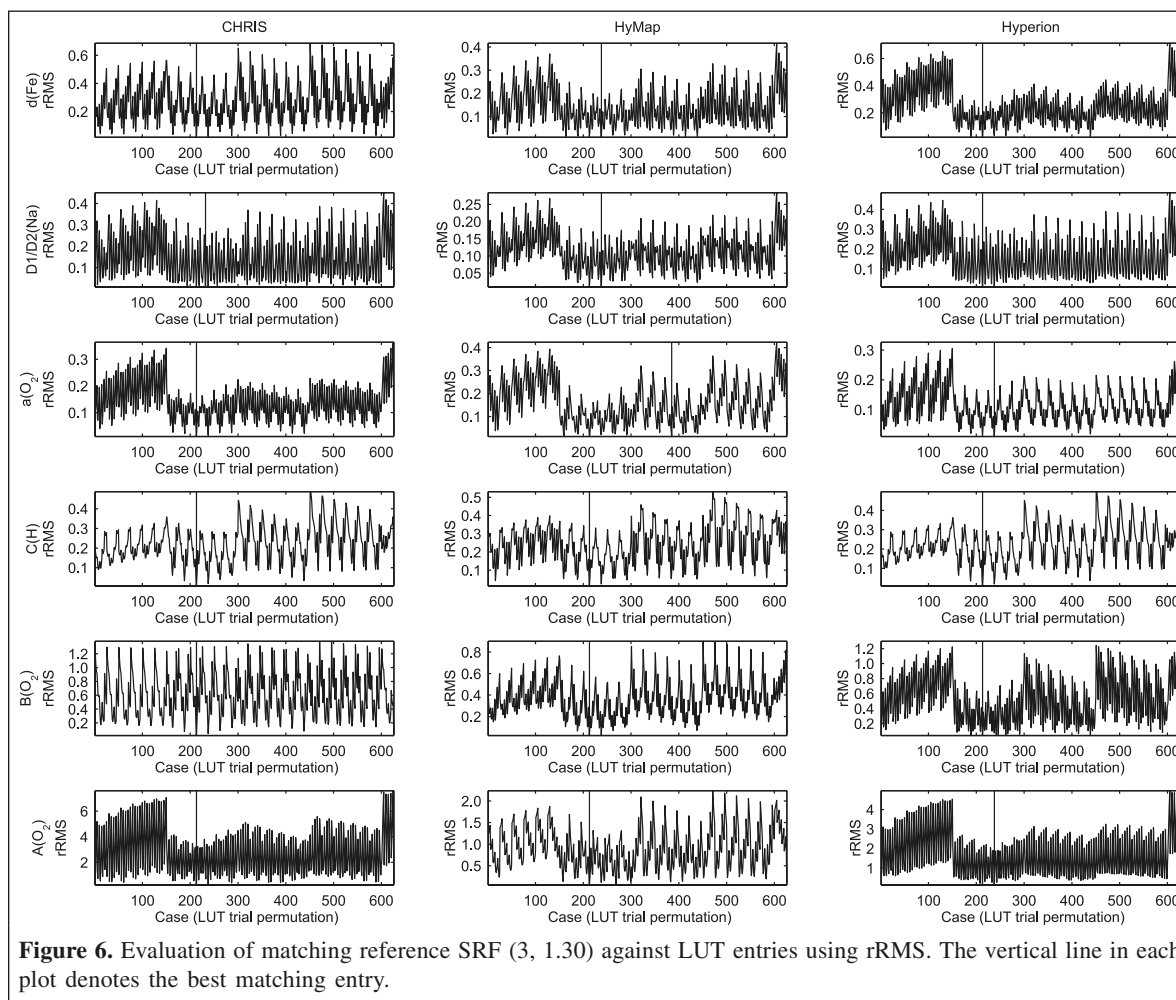
cause discernment difficulties, especially in the presence of noise.

Given the reference SRFs selected for this experiment, 11% (6 out of 54) of the SRF matches are inconclusive because the selection of best match is split among the feature windows tested. In 44% of the SRF matches, at least one result did not agree with the majority.

Discussion

Effectiveness of the method

It is both positive and surprising that a majority of the 54 evaluation samples unanimously agree on the best matching result, and yet the negative results show how precarious this success might really be in some cases. If one were presented only with graphs of the differences in spectra matching (**Figure 6**), it would be difficult to predict that the a(O) feature would be the case to consistently cause trouble. Intuitively, it would seem the best situation when groups of results steadily rise or fall, as in d(Fe) cases 1–150 for HyMap and Hyperion: one would expect that the trend implies where the best match is to be found. In the worst case, all groups hover in flat trends

such as in the D1/D2(Na) CHRIS and Hyperion cases 200–600. Not only are the groups flat, but also it appears that about 20% of the values could compete with each other for the best match, especially when there is unpredictable noise. On the other hand, it is not required that every Fraunhofer feature yield a clearly successful match. Statistical methods might be applicable for allowing stronger neighbouring windows to compensate for the results of the less prominent matches. It could also be that partial knowledge of the instrument (e.g., if it is likely to be summed) or knowledge of the underlying sensors reveals some subchannel insight that might play a role in dismissing unlikely combinations to help reduce the search space.

One very promising result is revealed by examining the A(O) case across all instruments. Upon revisiting **Figure 4**, it is interesting to see that the third channel in the two instrument-specific A(O) windows for CHRIS and Hyperion line up almost exactly and seem to be quite near to the trough of the feature between 760 and 765 nm. However, HyMap not only does not line up with the other two instruments but also does not seem to have any band that contains the trough as its primary constituent, as can be seen by the relative similarity of the value ranges of the second and third channels in the feature. Nevertheless, the retrieval method seems to do well enough at

Table 4. Mean ($\bar{x}$) and standard deviation (σ) of rRMS for the reference spectra.

(A) CHRIS

	3, 1.30		3, 1.44		3, 1.58		3, 1.72		3, 1.86		3, 2.00	
	$\bar{x}$	σ	$\bar{x}$	σ	$\bar{x}$	σ	$\bar{x}$	σ	$\bar{x}$	σ	$\bar{x}$	σ
d(Fe)	0.27	0.14	0.27	0.14	0.28	0.15	0.29	0.16			0.31	0.18
D1/D2(Na)	—	—	0.15	0.09	0.15	0.09	—	—			0.18	0.11
a(O)	0.14	0.06	0.14	0.06	0.15	0.06	0.16	0.07			0.18	0.08
C(H)	0.22	0.09	0.22	0.09	0.22	0.10	0.22	0.10			0.23	0.11
B(O)	0.61	0.31	0.61	0.31	0.62	0.31	0.62	0.32			0.63	0.33
A(O)	2.69	1.61	2.71	1.57	2.81	1.61	—	—			3.39	1.93

	5, 1.30		5, 1.44		5, 1.58		5, 1.72		5, 1.86		5, 2.00	
	$\bar{x}$	σ	$\bar{x}$	σ	$\bar{x}$	σ	$\bar{x}$	σ	$\bar{x}$	σ	$\bar{x}$	σ
d(Fe)	—	—	0.29	0.15	0.28	0.14	0.27	0.14	0.27	0.14	0.27	0.14
D1/D2(Na)	0.16	0.11	0.16	0.11	0.16	0.10	0.15	0.10	0.15	0.10	—	—
a(O)	0.16	0.09	0.15	0.09	0.14	0.08	0.14	0.08	0.14	0.07	0.14	0.06
C(H)	—	—	0.23	0.09	0.23	0.09	0.22	0.09	0.22	0.09	0.22	0.09
B(O)	0.62	0.35	0.62	0.33	0.61	0.32	0.61	0.32	0.61	0.31	0.61	0.31
A(O)	3.07	2.04	2.97	1.95	2.87	1.85	2.78	1.75	2.72	1.67	2.69	1.61

	7, 1.30		7, 1.44		7, 1.58		7, 1.72		7, 1.86		7, 2.00	
	$\bar{x}$	σ	$\bar{x}$	σ	$\bar{x}$	σ	$\bar{x}$	σ	$\bar{x}$	σ	$\bar{x}$	σ
d(Fe)	0.33	0.17	0.32	0.17	0.31	0.16	0.30	0.15	0.29	0.15	0.28	0.14
D1/D2(Na)	0.18	0.12	0.17	0.11	0.17	0.11	—	—	0.16	0.11	0.16	0.10
a(O)	0.17	0.10	0.17	0.10	—	—	—	—	0.15	0.09	0.15	0.09
C(H)	0.26	0.11	0.25	0.11	0.24	0.10	0.24	0.10	0.23	0.09	0.23	0.09
B(O)	0.64	0.36	0.63	0.36	0.63	0.35	0.62	0.35	0.62	0.34	0.61	0.33
A(O)	3.27	2.19	3.22	2.16	3.15	2.11	3.08	2.05	3.00	1.98	2.92	1.91

(B) HyMap

	3, 1.30		3, 1.44		3, 1.58		3, 1.72		3, 1.86		3, 2.00	
	$\bar{x}$	σ	$\bar{x}$	σ	$\bar{x}$	σ	$\bar{x}$	σ	$\bar{x}$	σ	$\bar{x}$	σ
d(Fe)			0.14	0.07	0.14	0.08	0.15	0.08	—	—	0.17	0.09
D1/D2(Na)			0.11	0.05	0.12	0.05	0.13	0.05	0.13	0.06	0.14	0.06
a(O)			0.17	0.08	0.18	0.09	—	—	—	—	0.23	0.12
C(H)			0.24	0.11	0.25	0.12	0.26	0.13	0.27	0.13	0.28	0.14
B(O)			0.36	0.16	0.37	0.17	0.38	0.18	0.40	0.19	0.42	0.21
A(O)			0.90	0.48	0.94	0.52	1.00	0.57	1.05	0.61	1.11	0.65

	5, 1.30		5, 1.44		5, 1.58		5, 1.72		5, 1.86		5, 2.00	
	$\bar{x}$	σ	$\bar{x}$	σ	$\bar{x}$	σ	$\bar{x}$	σ	$\bar{x}$	σ	$\bar{x}$	σ
d(Fe)			0.15	0.09	0.14	0.08	0.14	0.08	0.14	0.08	0.14	0.08
D1/D2(Na)			0.12	0.06	0.11	0.06	—	—	0.11	0.05	0.11	0.05
a(O)			0.18	0.12	0.17	0.11	0.16	0.10	0.16	0.09	—	—
C(H)			0.25	0.11	0.25	0.10	0.24	0.10	0.24	0.10	0.24	0.10
B(O)			0.39	0.18	0.38	0.17	0.37	0.17	0.37	0.16	0.36	0.16
A(O)			0.98	0.54	0.94	0.51	0.91	0.48	0.89	0.46	0.89	0.46

	7, 1.30		7, 1.44		7, 1.58		7, 1.72		7, 1.86		7, 2.00	
	$\bar{x}$	σ	$\bar{x}$	σ	$\bar{x}$	σ	$\bar{x}$	σ	$\bar{x}$	σ	$\bar{x}$	σ
d(Fe)	0.17	0.10	0.16	0.10	0.15	0.10			0.15	0.09	0.14	0.09
D1/D2(Na)	0.13	0.07	0.13	0.07	0.12	0.07			0.12	0.06	0.12	0.06
a(O)	0.22	0.15	—	—	0.20	0.14			0.18	0.13	0.17	0.12
C(H)	0.31	0.14	0.29	0.13	0.28	0.13			0.26	0.11	0.25	0.11
B(O)	0.42	0.18	0.42	0.18	0.41	0.18			0.39	0.18	0.38	0.17
A(O)	1.14	0.66	1.10	0.63	1.06	0.61			0.99	0.55	0.96	0.52

Table 4 (*concluded*).

(C) Hyperion

	3, 1.30		3, 1.44		3, 1.58		3, 1.72		3, 1.86		3, 2.00	
	$\bar{x}$	σ	$\bar{x}$	σ	$\bar{x}$	σ	$\bar{x}$	σ	$\bar{x}$	σ	$\bar{x}$	σ
d(Fe)	0.26	0.13	0.27	0.12	0.29	0.12	—	—	—	—	0.36	0.17
D1/D2(Na)	0.16	0.10	0.16	0.09	0.17	0.09	0.18	0.09	0.19	0.09	0.20	0.09
a(O)	—	—	0.12	0.05	0.12	0.06	0.13	0.06	0.14	0.07	0.14	0.07
C(H)	0.22	0.09	0.22	0.09	0.22	0.10	0.23	0.10	0.23	0.11	0.24	0.11
B(O)	0.53	0.29	0.55	0.30	0.58	0.33	0.63	0.37	—	—	0.71	0.43
A(O)	—	—	1.71	0.97	1.79	0.96	1.91	1.01	2.06	1.09	2.22	1.18

	5, 1.30		5, 1.44		5, 1.58		5, 1.72		5, 1.86		5, 2.00	
	$\bar{x}$	σ	$\bar{x}$	σ	$\bar{x}$	σ	$\bar{x}$	σ	$\bar{x}$	σ	$\bar{x}$	σ
d(Fe)			0.27	0.20	0.26	0.18	0.26	0.16	0.25	0.15	0.26	0.13
D1/D2(Na)			0.17	0.11	0.17	0.10	0.17	0.10	0.17	0.10	—	—
a(O)			0.12	0.07	0.12	0.07	0.12	0.06	0.12	0.06	0.12	0.06
C(H)			—	—	0.23	0.09	0.23	0.09	0.22	0.09	0.22	0.09
B(O)			0.59	0.39	0.55	0.35	0.53	0.32	0.52	0.30	—	—
A(O)			1.82	1.27	1.78	1.22	1.73	1.16	1.70	1.10	1.69	1.04

	7, 1.30		7, 1.44		7, 1.58		7, 1.72		7, 1.86		7, 2.00	
	$\bar{x}$	σ	$\bar{x}$	σ	$\bar{x}$	σ	$\bar{x}$	σ	$\bar{x}$	σ	$\bar{x}$	σ
d(Fe)	0.33	0.23	0.32	0.23	0.30	0.22			0.28	0.20	0.27	0.19
D1/D2(Na)	0.18	0.11	0.18	0.11	0.18	0.11			—	—	0.17	0.11
a(O)	0.14	0.08	0.14	0.08	0.13	0.08			0.13	0.08	0.12	0.07
C(H)	0.27	0.11	0.26	0.11	—	—			0.24	0.09	0.23	0.09
B(O)	0.79	0.52	0.73	0.49	0.67	0.46			—	—	0.57	0.37
A(O)	1.94	1.34	1.92	1.34	1.90	1.32			1.84	1.28	1.80	1.25

Note: Blanks in the table indicate that the best match is not clear, and the em-dashes (—) indicate that the best match is not the one agreed upon by the other features.

providing a clearly matching spectra. The positive conclusion from this is that, at least in some cases, the width and prominence of a feature can be more important in deciding discernibility than the placement and interval of the band of a given instrument. Another interesting observation from the same feature is to compare **Figure 4** with the bottom row of **Figure 6**. CHRIS and Hyperion produce similar signatures in the LUT, seemingly due to the similar shape of the spectra in the window, even though the SSIs of the two instruments are clearly different. The signature in the LUT for HyMap for this case is the other extreme.

Integration within processing chain

In addition to validating the method and iteratively refining its currently nominal components, the method and its components must also integrate well within a complete processing chain. Such a processing chain has been refined over many years by three of the authors for preprocessing hyperspectral data such as acquired by EO-1 Hyperion (Khurshid et al., 2006). In that chain, a noise-reduction step involving the average-smooth tool of the imaging spectrometer data analysis system (ISDAS) (Staenz et al., 1998) is already performed in preparation for an existing spectral smile detection step. The results of this noise reduction could be used unaltered as input to a revised spectral smile and SRF detection

module. In fact, the existing smile detection module already not only detects smile but also band-centre and bandwidth shifts and gain–offset detection in an iterative feedback loop coupled with atmospheric correction, since these all need to be performed simultaneously. It is this module that would need to incorporate the additional SRF parameterization and window-based spectrum-matching components proposed here. Broad coverage over the range of the instrument and statistical consistency tests are already implemented by the current module. The newly retrieved SRFs would then be added to the already retrieved band-centre and bandwidth parameters as input for the immediately following atmospheric correction module. Smile correction, if needed, would occur following atmospheric correction.

Conclusions

The theoretical discernibility of spectral response function (SRF) shapes has been confirmed using more practical shapes than those of the abstract functions from a previous study (Brazile et al., 2006). In particular, it appears feasible to fully cover a continuous range of symmetric shapes from Gaussian to boxcar. Although the Tukey SRF parameterization appears interesting because of its smoothness, it has been rejected for its inability to cover shapes closer to the often-specified
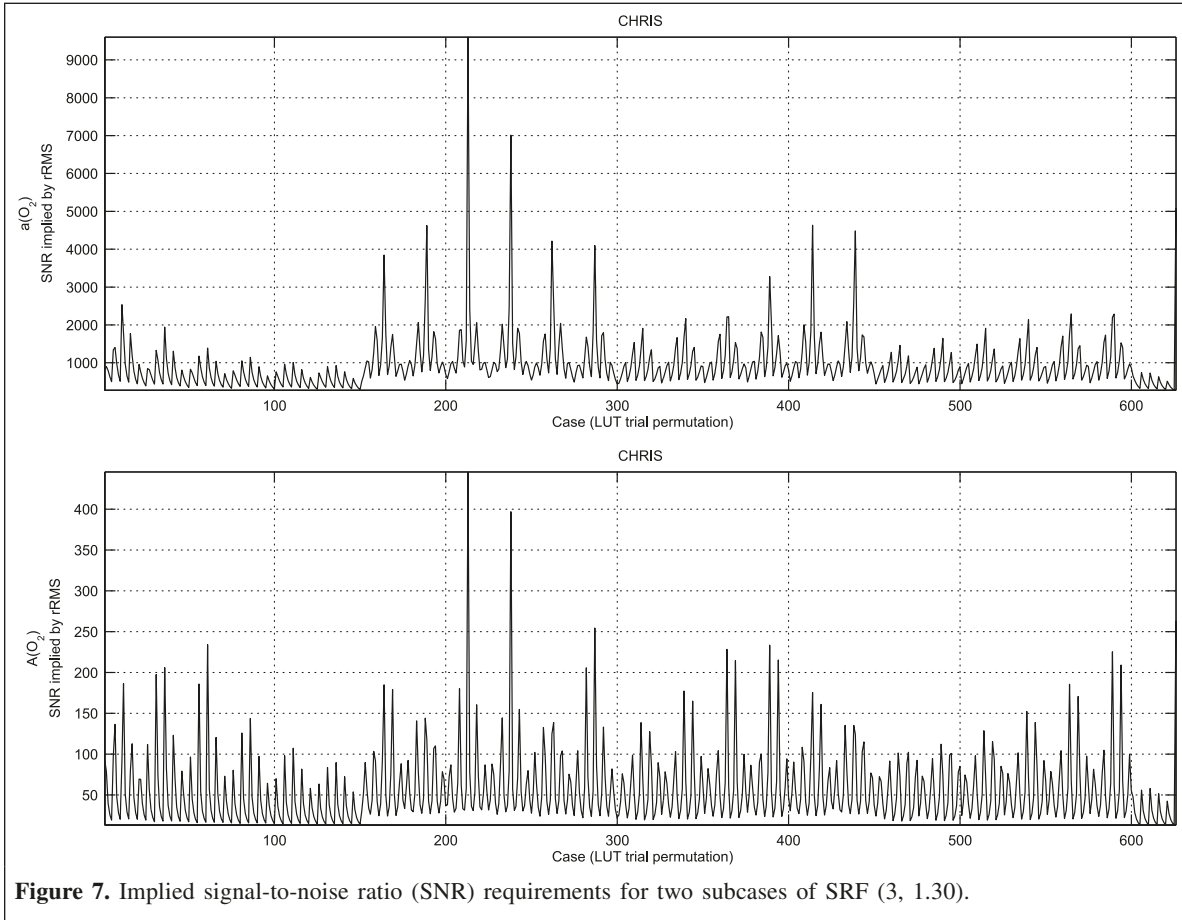
Figure 7. Implied signal-to-noise ratio (SNR) requirements for two subcases of SRF (3, 1.30).

Table 5. Conservative SNR requirements (1 : 500, 1 : 1 000, 1 : 5 000, 1: 10 000, 1 : 50 000, and 1 : ∞) implied by simulation.

(A) CHRIS

	3, 1.30	3, 1.44	3, 1.58	3, 1.72	3, 1.86	3, 2.00
d(Fe)	10 000	5 000	5 000	10 000		5 000
D1/D2(Na)	—	5 000	5 000	—		5 000
a(O)	50 000	5 000	5 000	10 000		5 000
C(H)	5 000	5 000	5 000	5 000		5 000
B(O)	5 000	5 000	1000	1000		1000
A(O)	5 000	500	500	—		500

	5, 1.30	5, 1.44	5, 1.58	5, 1.72	5, 1.86	5, 2.00
d(Fe)	—	5 000	10 000	50 000	5 000	50 000
D1/D2(Na)	50 000	50 000	50 000	50 000	50 000	—
a(O)	10 000	10 000	10 000	50 000	10 000	50 000
C(H)	—	10 000	5 000	∞	10 000	50 000
B(O)	5 000	5 000	5 000	10 000	5 000	10 000
A(O)	5 000	500	5 000	5 000	500	5 000

	7, 1.30	7, 1.44	7, 1.58	7, 1.72	7, 1.86	7, 2.00
d(Fe)	5 000	50 000	50 000	∞	50 000	10 000
D1/D2(Na)	10 000	50 000	50 000	—	50 000	10 000
a(O)	5 000	50 000	—	—	50 000	10 000
C(H)	5 000	50 000	50 000	50 000	50 000	10 000
B(O)	5 000	50 000	5 000	50 000	10 000	5 000
A(O)	1 000	5 000	5 000	50 000	5 000	500

Table 5 (*concluded*).

(B) HyMap

	3, 1.30	3, 1.44	3, 1.58	3, 1.72	3, 1.86	3, 2.00
d(Fe)		5 000	5 000	10 000	—	5 000
D1/D2(Na)		5 000	5 000	10 000	5 000	5 000
a(O)		5 000	5 000	—	—	5 000
C(H)		5 000	5 000	5 000	5 000	5 000
B(O)		5 000	1 000	1 000	5 000	1 000
A(O)		1 000	500	1 000	5 000	500
	5, 1.30	5, 1.44	5, 1.58	5, 1.72	5, 1.86	5, 2.00
d(Fe)		5 000	10 000	50 000	5 000	50 000
D1/D2(Na)		50 000	50 000	—	50 000	50 000
a(O)		10 000	10 000	50 000	10 000	—
C(H)		10 000	5 000	∞	10 000	50 000
B(O)		5 000	5 000	10 000	5 000	10 000
A(O)		5 000	5 000	10 000	5 000	10 000
	7, 1.30	7, 1.44	7, 1.58	7, 1.72	7, 1.86	7, 2.00
d(Fe)	5 000	50 000	50 000		50 000	10 000
D1/D2(Na)	10 000	50 000	50 000		50 000	10 000
a(O)	5 000	—	50 000		50 000	10 000
C(H)	5 000	50 000	50 000		50 000	10 000
B(O)	5 000	50 000	5 000		10 000	5 000
A(O)	1 000	10 000	5 000		5 000	5 000

(C) Hyperion

	3, 1.30	3, 1.44	3, 1.58	3, 1.72	3, 1.86	3, 2.00
d(Fe)	10 000	5 000	5 000	—	—	5 000
D1/D2(Na)	50 000	5 000	5 000	10 000	5 000	5 000
a(O)	—	5 000	5 000	10 000	50 000	5 000
C(H)	5 000	5 000	5 000	5 000	5 000	5 000
B(O)	5 000	5 000	1 000	1 000	—	1 000
A(O)	—	500	500	500	500	500
	5, 1.30	5, 1.44	5, 1.58	5, 1.72	5, 1.86	5, 2.00
d(Fe)		5 000	10 000	50 000	5 000	50 000
D1/D2(Na)		50 000	50 000	50 000	50 000	—
a(O)		10 000	10 000	50 000	10 000	50 000
C(H)		—	5 000	∞	10 000	50 000
B(O)		5 000	5 000	10 000	5 000	—
A(O)		1 000	5 000	5 000	1 000	50 000
	7, 1.30	7, 1.44	7, 1.58	7, 1.72	7, 1.86	7, 2.00
d(Fe)	5 000	50 000	50 000		50 000	10 000
D1/D2(Na)	10 000	50 000	50 000		—	10 000
a(O)	5 000	50 000	50 000		50 000	10 000
C(H)	5 000	50 000	—		50 000	10 000
B(O)	5 000	50 000	5 000		—	5 000
A(O)	5 000	5 000	5 000		5 000	1 000

Note: See the note to **Table 4**.

Gaussian. The feasibility of using a summed Gaussian with subchannel full width at half-maximum (FWHM) to spectral sampling interval (SSI) ratio parameterization shows promise in its shape coverage in the limited trials presented here. The robustness of this parameterization and the use of relative root mean square (rRMS) as spectrum-matching metric are suggested as nominal implementations of proposed SRF retrieval components because of the ability to match even in the presence of band-centre and bandwidth deviations. However, less smooth parameterization in two dimensions may prove to be a detriment when attempting to approach higher levels of retrieval accuracy. An additional promising result with this nominal implementation is that all but 4% of the combinations of sensor and single feature Fraunhofer windows presented
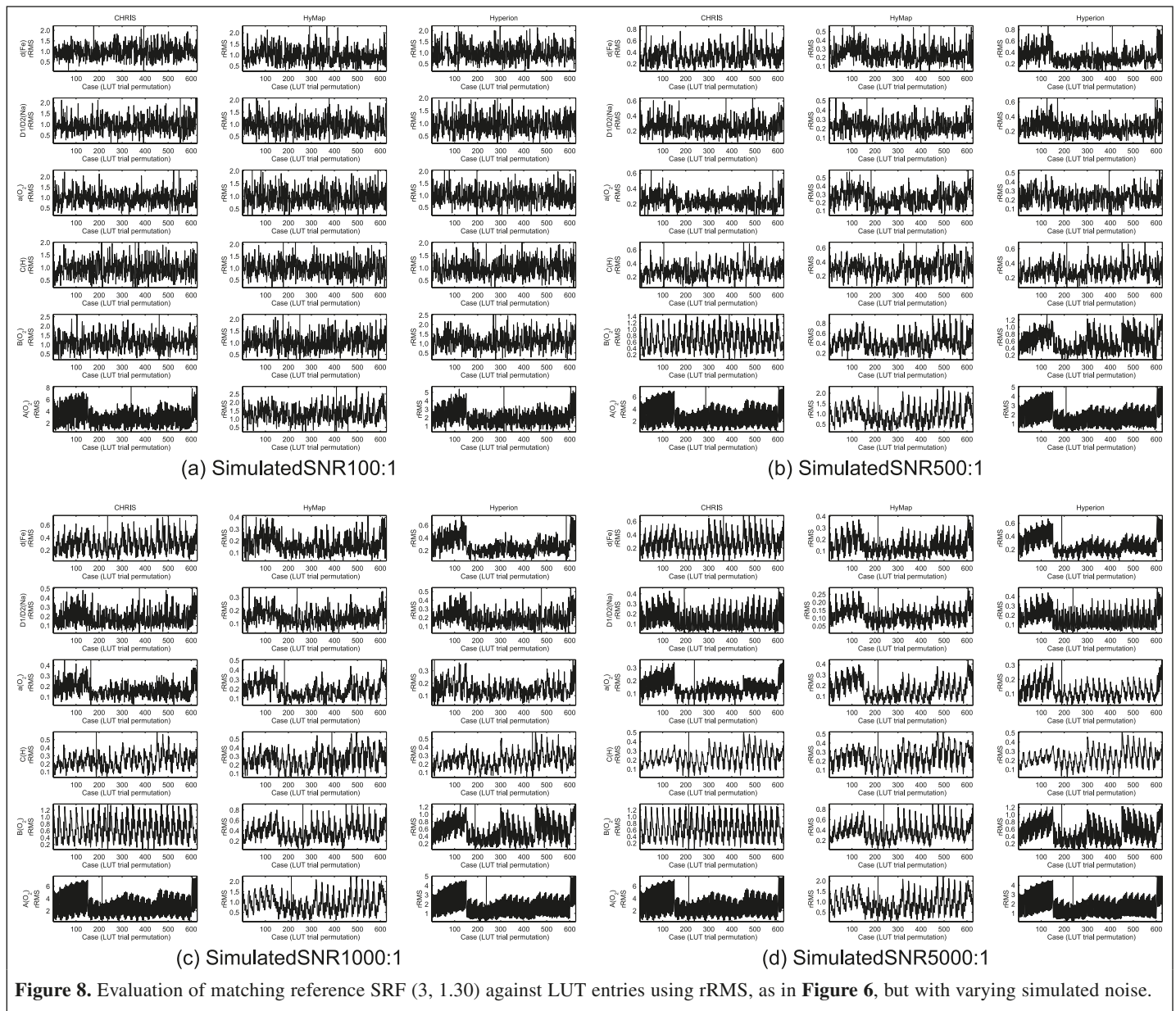
Figure 8. Evaluation of matching reference SRF (3, 1.30) against LUT entries using rRMS, as in **Figure 6**, but with varying simulated noise.

here provide a statistically successful outcome. This holds promise for supporting SRF retrieval throughout a nontrivial subset of the entire spectral range of an instrument. Clearly, some features reveal more prominent signal discernment than others, but the basic method is expected to be applicable even in weaker cases, assuming the components of the proposed method improve over time, along with the use of signal-to-noise enhancement such as along-track averaging.

Lastly, the general applicability of the method of spectrum matching for SRF characterization is promising, as three clearly different instruments (CHRIS, HyMap, and Hyperion) yielded uniformly positive results, even though the feature window sizes and locations relative to the feature centres varied greatly.

It is suggested that the method, even in its currently primitive form, could be used to obtain SRF estimates better than

Gaussian for the not-uncommon case in which bands are created by summing up to tens of subchannels.

At the same time, it is noted that these conclusions have been based on a limited set of trials and that further research is required to substantiate them.

Acknowledgments

References

Anger, C., Achal, S., Ivanco, T., Mah, S., Price, R., and Busler, J. 1996. Extended operational capabilities of *casi*. In *Proceedings of the 2nd International Airborne Remote Sensing Conference*, June 1996, San Francisco, Calif. Environmental Research Institute of Michigan (ERIM) International, Ann Arbor, Mich. pp. 124–133.

Barnsley, M.J., Settle, J., Cutter, M., Lobb, D., and Teston, F. 2004. The PROBA/CHRIS mission: a low-cost smallsat for hyperspectral, multi-angle observations of the earth surface and atmosphere. *IEEE Transactions on Geoscience and Remote Sensing*, Vol. 42, pp. 1512–1520.

Beckles, B., Son, S.-C., and Kewley, J. 2005. Current methods for negotiating firewalls for the Condor system. In *Proceedings of the 4th UK e-Science All Hands Meeting (AHM'05)*, September 2005, Nottingham, UK. Edited by S. Cox and D.W. Walker. Engineering and Physical Sciences Research Council (EPSRC), Swindon, UK.

Berk, A., Bernstein, L.S., Anderson, G.P., Acharya, P.K., Robertson, D.C., Chetwynd, J.H., and Adler-Golden, S.M. 1998. MODTRAN cloud and multiple scattering upgrades with application to AVIRIS. *Remote Sensing of Environment*, Vol. 65, No. 3, pp. 367–375.

Berk, A., Anderson, G., Acharay, P., Hoke, M., Chetwynd, J., Bernstein, L., Shettle, E., Matthew, M., and Adler-Golden, S. 2003. *MODTRAN 4 version 3 revision 1 user's manual*. Air Force Research Laboratory (AFRL), Space Vehicles Directorate, Air Force Material Command, Hanscom AFB, Hanscom, Mass. AFRL Technical Report.

Brazile, J. 2005. *MODTRAN-compatible SRF generator* [online]. Available from www.mathworks.com/matlabcentral/fileexchange/loadFile.do?objectId = 8723 [accessed January 2005].

Brazile, J. 2006. *Low fat grid* [online] Available from code.google.com/p/lowfatgrid/ [accessed November 2006].

Brazile, J., Neville, R.A., Staenz, K., Schläpfer, D., Sun, L., and Itten, K.I. 2006. Scene-based spectral response function shape discernibility for the APEX imaging spectrometer. *IEEE Geoscience and Remote Sensing Letters*, Vol. 3, pp. 414–418.

Casadio, S., and Colagrande, P. 2004. Meris O2 calibration using sciamachy measurements. In *Proceedings of the MERIS User Workshop*, 10–13 November 2003, Frascati, Italy. CD-ROM. European Space Agency (ESA) Publications Division, ESTEC, Noordwijk, The Netherlands. ESA Report SP-549.

Cocks, T., Jenssen, R., Stewart, A., Wilson, I., and Shields, T. 1998. The HyMap(TM) airborne hyperspectral sensor: the system, calibration and performance. In *Proceedings of the 1st EARSeL Workshop on Imaging Spectroscopy*, 6–8 October 1998, Zurich, Switzerland. EARSeL Secretariat, Paris. pp. 37–42.

Gao, B.-C., Montes, M.J., and Davis, C.O. 2002. A curve-fitting technique to improve wavelength calibrations of imaging spectrometer data. In *Proceedings of the 11th JPL Airborne Earth Science Workshop*, 4–8 March 2002, Pasadena, Calif. Edited by R.O. Green. Jet Propulsion Laboratory (JPL) Publications, Pasadena, Calif. JPL Publication 03-4, pp. 99–105.

Gao, B.-C., Montes, M.J., and Davis, C.O. 2004. Refinement of wavelength calibrations of hyperspectral imaging data using a spectrum-matching technique. *Remote Sensing of Environment*, Vol. 90, pp. 424–433.

Godknecht, A.J., and Bolliger, C. 2004. *University of Zurich Matterhorn cluster* [online]. Available from www.matterhorn.unizh.ch [accessed September 2004].

Green, R.O., Eastwood, M.L., Sarture, C.M., Chrien, T., Aronsson, M., Chippendale, B., Faust, J., Pavri, B., Chovit, C., Solis, M., Olah, M., and Williams, O. 1988. Imaging spectrometry and the Airborne Visible / Infrared Imaging Spectrometer (AVIRIS). *Remote Sensing of Environment*, Vol. 65, pp. 227–248.

Harris, F.J. 1978. On the use of windows for harmonic analysis with the discrete fourier transform. *Proceedings of the IEEE*, Vol. 66, No. 1, pp. 51–83.

Itten, K.I., Schaepman, M., De Vos, L., Hermans, L., Schläepfer, H., and Droz, F. 1997. APEX — airborne prism experiment: a new concept for an airborne imaging spectrometer. In *Proceedings of the 3rd International Airborne Remote Sensing Conference and Exhibition*, 3–7 July 1997, Copenhagen. Environmental Research Institute of Michigan (ERIM) International, Ann Arbor, Mich. Vol. 1, pp. 181–188.

Khurshid, K.S., Staenz, K., Sun, L., Neville, R., White, H.P., Bannari, A., Champagne, C.M., and Hitchcock, R. 2006. Preprocessing of EO-1 Hyperion data. *Canadian Journal of Remote Sensing*, Vol. 32, No. 2, pp. 84–97.

Litzkow, M.J., Livny, M., and Mutka, M.W. 1988. Condor — a hunter of idle workstations. In *Proceedings of the 8th International Conference on Distributed Computing Systems*, 13–17 June 1988, San Jose, Calif. IEEE Computer Society Press, Los Alamitos, Calif. pp. 104–111.

Milton, E.J. 2006. *Casi-2 sensor data acquisition modes* [online]. Available from arsf.nerc.ac.uk/documents/casi2.pdf [accessed November 2006].

Milton, E.J., and Choi, K.Y. 2004. Estimating the spectral response function of the *casi*-2. In *Proceedings of the Annual Conference of the Remote Sensing and Photogrammetry Society*, Aberdeen, Scotland. CD-ROM. Remote Sensing and Photogrammetry Society, Nottingham, UK.

Neville, R.A. 2003. *Spectral absorption features for use in calibrating imaging spectrometers*. Canada Centre for Remote Sensing, Natural Resources Canada, Ottawa, Ont. Technical Report CHTN_2003_002. 11 pp.

Neville, R.A., Sun, L., and Staenz, K. 2003. Detection of spectral line curvature in imaging spectrometer data. In *Proceedings of the SPIE Conference on Algorithms and Technologies for Multispectral, Hyperspectral, and Ultraspectral Imagery IX*, April 2003, Orlando, Fla. Edited by S.S. Shen and P.E. Lewis. The International Society for Optical Engineering (SPIE), Bellingham, Wash. Proceedings of SPIE Volume 5093, pp. 144–154.

Neville, R.A., Sun, L., and Staenz, K. 2004. Detection of keystone in imaging spectrometer data. In *Proceedings of the SPIE Conference on Algorithms and Technologies for Multispectral, Hyperspectral, and Ultraspectral Imagery X*, 12–15 April 2004, Orlando, Fla. Edited by S.S. Shen and P.E. Lewis. The International Society for Optical Engineering (SPIE), Bellingham, Wash. Proceedings of SPIE Volume 5425, pp. 208–217.

Nieke, J., Itten, K., Debruyn, W., Kaiser, J., Schläpfer, D., Brazile, J., Meuleman, K., Kempeneers, P., Neukom, A., Schilliger, T., De Vos, L., Piesbergen, J., Gege, P., Suhr, B., Schaepman, M., Gavira, J., Ulbrich, G., and Meynart, R. 2005. The airborne imaging spectrometer APEX: from concept to realization. In *Proceedings of the 4th EARSeL Workshop on Imaging Spectroscopy*, 27–30 April 2005, Warsaw, Poland. Edited by B. Zagajewski and M. Sobczak. EARSeL Secretariat, Paris. pp. 67–74.

Palatin, N., and Kliot, G. 2003. *Low latency invocation in condor*. Computer Science Department, Technion – Israel Institute of Technology, Haifa, Israel. Technical Report. 22 pp.

Pearlman, J.P., Barry, P., Segal, C., Shepanksi, J., Beiso, D., and Carman, S. 2003. Hyperion, a space-based imaging spectrometer. *IEEE Transactions on Geoscience and Remote Sensing*, Vol. 41, No. 6, pp. 1160–1173.

Ramon, D., Santer, R.P., and Dubuisson, P. 2003. MERIS in-flight spectral calibration in O absorption using surface pressure retrieval. In *Optical Remote Sensing of the Atmosphere and Clouds III*. Edited by H.-L. Huang, D. Lu, and Y. Sasano. The International Society for Optical Engineering (SPIE), Bellingham, Wash. Proceedings of SPIE Volume 4891, pp. 505–514.

Rothman, L., Barbe, A., Benner, D.C., Brown, L., Camy-Peyret, C., Carleer, M., Chance, K., Clerbaux, C., Dana, V., Devi, V., Fayt, A., Flaud, J.-M., Gamache, R., Goldman, A., Jacquemart, D., Jucks, K., Lafferty, W., Mandin, J.-Y., Massie, S., Nemtchinov, V., Newnham, D., Perrin, A., Rinsland, C., Schroeder, J., Smith, K., Smith, M., Tang, K., Toth, R., Auwera, J.V., Varanasi, P., and Yoshino, K. 2003. The HITRAN molecular spectroscopic database: edition of 2000 including updates through 2001. *Journal of Quantitative Spectroscopy and Radiative Transfer*, Vol. 82, pp. 5–44.

Schaepman, M., and Itten, K. 1998. APEX-airborne PRISM experiment: an airborne imaging spectrometer serving as a precursor instrument of the future ESA land surface processes and interactions mission. In *Proceedings of the ISPRS Commission VII Symposium on Resource and Environmental Monitoring*, 1–4 September 1998, Budapest, Hungary. International Archives of Photogrammetry and Remote Sensing, Enschede, The Netherlands. Vol. 22, Part 7, pp. 31–37.

Sinclair, P., Berman, R., Hersom, C., and Hollinger, A. 2002. Spectral calibration of hyperspectral imagers using a white light etalon. In *Proceedings of the 12th CASI Conference on Astronautics (ASTRO 2002)*, 12–14 November 2002, Ottawa, Ont. CD-ROM. Canadian Aeronautics and Space Institute (CASI), Ottawa, Ont.

Smith, S.W. 1997. *The scientist's and engineer's guide to digital signal processing*. California Technical Publishers, San Diego, Calif.

Staenz, K., Szeredi, T., and Schwarz, J. 1998. ISDAS — a system for processing/analyzing hyperspectral data. *Canadian Journal of Remote Sensing*, Vol. 24, No. 2, pp. 99–113.

Thuillier, G., Hersé, M., Labs, D., Foujols, T., Peetermans, W., Gillotay, D., Simon, P.C., and Mandel, H. 2003. The solar spectral irradiance from 200 to 2400 nm as measured by the SOLSPEC spectrometer from the Atlas and Eureca missions. *Solar Physics*, Vol. 214, pp. 1–22.

Weisstein, E.W. 2005. *Full width at half maximum* [online]. Available from mathworld.wolfram.com/FullWidthatHalfMaximum.html [accessed January 2005].

Appendix A: Computational requirements

For reasons of scientific rigor and reproducibility, all SRF filtering in this experiment is performed directly by MODTRAN 4 using the "FLTNAM" parameter. However, for generating a LUT, this method results in a large amount of wasted effort, since the same base spectrum is recomputed for each of the hundreds of varying SRFs. In practice, a spectrum needs only to be modelled by MODTRAN once at high resolution for each base case (example as summarized in **Table 2**), and a separate, postprocessing convolution can be run to achieve the simulated instrument-filtered result for each of the varying SRFs.

Implementing this shortcut would lead to a more manageable operational process, especially when considering the number of MODTRAN executions that are required to cover common cases. Real cases require multiple step variation of several base parameters, e.g., multiple target reflectances, aerosol models, visibilities, atmospheric models, surface altitudes, and solar zenith angles.

A common solution for the batch operation of multiple executions of a single program with varying input parameters is the use of queuing software such as Condor (Litzkow et al., 1988), whose manual excerpt describing use of the "initialdir" and "queue" parameters is directly applicable to this situation. Unfortunately, Condor is not intended for low latency invocation, although experimental patches are available that provide this capability (Palatin and Kliot, 2003). In the MODTRAN configurations used in this study, roughly the same amount of time is spent in between executions as during the executions themselves, effectively doubling the total run time from the expected run time. For this reason, and because of the difficulty in operating across firewalls (Beckles et al., 2005), a simpler, hypertext transfer protocol (HTTP) based, "low fat grid" (Brazile, 2006) application is used for performing the cooperative sharing of computing resources at the disperse institutions.

List of abbreviations

AMD	Advanced Micro Devices
APEX	Airborne PRISM Experiment
ASCII	American standard code for information interchange
AVIRIS	Airborne Visible / Infrared Imaging Spectrometer
casi	Compact Airborne Spectrographic Imager
CHRIS	compact high-resolution imaging spectroscopy sensor
ESA	European Space Agency
FWHM	full width at half maximum
ISDAS	imaging spectrometer data analysis system
LUT	look-up table
MERIS	medium-resolution imaging spectrometer
MODTRAN	moderate-resolution transmittance code
RMS	root mean square
RT	radiative transfer
SNR	signal-to-noise ratio
SRF	spectral response function
SSI	spectral sampling interval